

Ballistic transport through quantum point contacts of multiorbital oxidesJ. Settino ¹, R. Citro ^{1,2,3}, F. Romeo ², V. Cataudella,^{4,5} and C. A. Perroni^{4,5}¹*CNR-SPIN c/o Università degli Studi di Salerno, I-84084 Fisciano (Sa), Italy*²*Dipartimento di Fisica “E. R. Caianiello,” Università degli Studi di Salerno, I-84084 Fisciano (Sa), Italy*³*INFN, Sezione di Napoli, 80126 Napoli NA, Italy*⁴*CNR-SPIN c/o Università degli Studi di Napoli Federico II, Complesso Universitario Monte S. Angelo, Via Cintia, I-80126 Napoli, Italy*⁵*Physics Department “Ettore Pancini,” Università degli Studi di Napoli Federico II, Complesso Universitario Monte S. Angelo, Via Cintia, I-80126 Napoli, Italy*

(Received 7 December 2020; revised 9 April 2021; accepted 28 May 2021; published 10 June 2021)

Linear and nonlinear transport properties through a quantum point contact based on oxides two-dimensional electron gas is examined using the tight-binding method and the $\mathbf{k} \cdot \mathbf{p}$ approach. The ballistic transport is analyzed in contacts realized at the (001) interface between band insulators LaAlO_3 and SrTiO_3 by using the Landauer-Büttiker method for many sub-bands derived from three Ti $3d$ orbitals (d_{yz} , d_{zx} , and d_{xy}) in the presence of an out-of-plane magnetic field. We focus especially on the role played by the atomic spin-orbit coupling and the inversion-symmetry-breaking term. Three different transport regimes stem out: The first, at low energies, involving the first d_{xy} -like sub-bands, where the conductance quantization is clearly observed; a second one, at intermediate energies, entailing further d_{xy} -like sub-bands, where the sub-band splitting induced by the magnetic field is quenched; the third one, where the mixing between light d_{xy} -like, heavy d_{yz} -like, and d_{zx} -like sub-bands is so strong that the conductance plateaus turn out to be very narrow. Very good agreement is found with recent experiments exploring the transport properties at low energies.

DOI: [10.1103/PhysRevB.103.235120](https://doi.org/10.1103/PhysRevB.103.235120)**I. INTRODUCTION**

Since the first evidence of the conductance quantization in 1988 [1], quantum point contacts (QPCs) have played a relevant role in mesoscopic physics. In fact, they naturally offer evidence of the quantum-mechanical nature of the charge carriers through a constriction whose width is comparable with the Fermi wavelength. The observation of well-defined plateaus in the conductance of the device, quantized in integer values of $2e^2/h$ (where e is the electron charge and h is Planck's constant), indicates ballistic transport involving a limited number of conduction channels which are spin degenerate [2]. The quantization of G can be explained from the formation of one-dimensional (1D) sub-bands in the constriction due to the lateral confinement. Then G is given by the Landauer-type formula [3] $G = 2Ne^2/h$, with N being the number of occupied 1D sub-bands. A detailed analysis has shown that a variation of the gate voltage V_G changes the width as well as the electron density of the constriction. Both mechanisms move the Fermi energy E_F in the channel through the 1D sub-bands and, whenever it passes a sub-band bottom, G changes by the quantized amount of $2e^2/h$.

Ballistic constrictions are routinely fabricated in semiconducting heterostructures such as $\text{AlGaAs}/\text{GaAs}$ [4] by means of a metallic split-gate, which, through the application of a negative gate voltage V_G , forms a constriction by electrostatic depletion. Moreover, the very low carrier density ($\approx 10^{11} \text{ cm}^{-2}$) results in large values of the Fermi wavelength λ_F ($\approx 50 \text{ nm}$), and the extreme cleanliness of these heterostructures also results in a large mean-free path that

can exceed several micrometers at low temperatures [5]. However, beyond these conventional materials, technological efforts have been put forward for the fabrication of nano-devices in thin films and heterostructures based on oxides exploiting the multifunctionality and the extreme sensitivity of these materials to external perturbations [6]. Recently, the two-dimensional electron gas (2DEG) formed at the (001) interface between band insulators LaAlO_3 and SrTiO_3 (LAO-STO) [7] has been much studied not only for its spin-orbit, multiband, and superconducting properties [8–12], but also for the possibility to realize nanostructures in the normal and superconducting state [13–15]. Moreover, recent theoretical works have suggested the 2DEGs at the LAO-STO interface as possible candidates for the realization of topological superconducting phases in quasi 1D nanowires [16–18]. However, in comparison with semiconductor-based heterostructures, this 2-DEG typically involves a higher carrier density ($\approx 10^{13} \text{ cm}^{-2}$) and has a reduced λ_F ($\approx 10\text{--}50 \text{ nm}$), imposing stronger constraints on the practical realization of such devices.

At the LAO-STO interface, the conduction band is formed by coupling the $t_{2g}3d$ orbitals (d_{xy} , d_{xz} , and d_{yz}) at neighboring Ti lattice sites through the $2p$ orbitals of the oxygen atoms. Under strong quantum confinement in the direction perpendicular to the interface, the degeneracy of the t_{2g} bands is lifted, resulting in a rich and complex band structure with discrete 2D states separated by typical energies of tens of meV [19,20]. The quantization of conductance in a ballistic QPC formed by electrostatic confinement of the LAO-STO

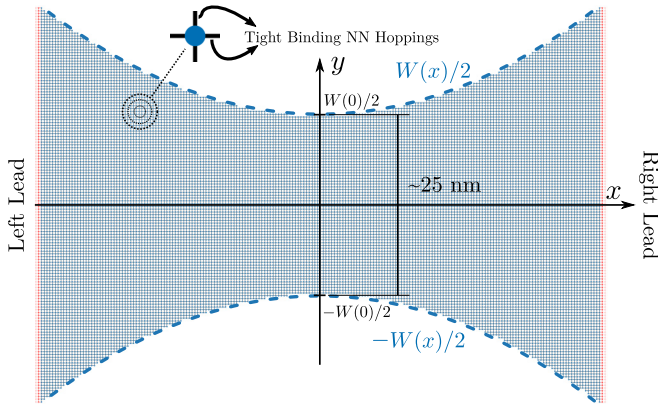


FIG. 1. Schematic view of the QPC simulated within the TB method. The thinnest size is made of 64 sites with a lattice constant $a = 0.39$ nm; the parabolic modulation of the transverse hard-wall confinement has a coefficient $\beta = 0.01$ nm $^{-1}$; the length of the TB system ensures the convergence of the results for the conductance.

2-DEG with a split gate was recently demonstrated in the normal state [15]. Moreover, the measurement of the g factor under a magnetic field applied in the direction normal to the interface was performed on the $n = 2$ conductance step, providing a value in the range 0.85–0.9, which differs from that of free electrons and is usually ascribed to the effect of strong spin-orbit coupling [9,21]. By adding a finite source-drain bias voltage V_B , a comprehensive spectroscopic study of the low energy levels inside the QPC was performed in the depleted regime [15]. However, while in the depleted regime, only the lowest d_{xy} energy bands are filled, at higher gate voltages or high carrier doping a multiband transport can occur and stronger features related to the multi-orbital nature of the subbands can emerge in the ballistic transport of oxide-based QPCs. This scenario encompasses the comprehension of two effects in the ballistic transport of oxide-based QPCs: The role of the atomic spin-orbit coupling and the inversion-symmetry-breaking term, that can break the picture of independent orbital channels and the multiband transport that takes place at higher doping densities.

In this paper, we theoretically analyze the ballistic transport through QPCs of multi-orbital 2DEG at the LAO-STO (001) interface modeling the normal-state constriction of 25 nm minimal size investigated in a recent experimental work [15]. To analyze the electronic structure of the QPC, we adopt both the $\mathbf{k} \cdot \mathbf{p}$ approach and the tight-binding (TB) method, including the effects of an applied magnetic field normal to the interface. In Fig. 1, we report a schematic view of the QPC simulated within the TB method with a curvature extracted from the recent experiment in Ref. [15]. We remark that the curvature is smooth, therefore the electron transport through the QPC is well within the so-called adiabatic regime [1,22]. Magnetoconductance and nonlinear transport properties have been calculated in the ballistic regime with analytical approaches appropriate for an adiabatic QPC at low carrier densities and with TB-based state-of-the-art numerical methods at all the densities, including multi-orbital effects.

We make a comparative analysis of the normal-state conductance, the differential conductance, and the transcon-

ductance in the absence and presence of a magnetic field normal to the interface finding three distinct ballistic transport regimes. The first one characterizes the low energy range since it involves only the first d_{xy} -like sub-bands. In the absence of magnetic field, the conductance is quantized in steps of $2e^2/h$, while, as expected, in the presence of the field, the conductance is quantized in steps of e^2/h . The second transport regime entails d_{xy} -like sub-bands at higher energies where standard strengths of the magnetic field do not induce a splitting of the sub-bands hampering the conductance quantization in steps of e^2/h . Within these two transport regimes, localized pin-like defects on the external sides of the QPC are able to induce conductance oscillations whose amplitude gets enhanced with increasing energy. Therefore, the conductance quantization is clearly visible in the first transport regime, while it gets altered in the second one. We point out that the theoretical results provide an accurate description for many features of the experimental data shown in Ref. [15], including also the presence of conductance oscillations. Finally, the third transport regime is at high energies where light d_{xy} -like strongly hybridize with heavy d_{yz} -like and d_{zx} -like sub-bands so that the conductance quantization is weak against external perturbations.

The paper is organized as follows. In Sec. II, the model Hamiltonian for an oxide strip is presented and its energy spectrum is discussed. In Sec. III, the low-energy transport is investigated by using analytical approaches. In Sec. IV, the transport is examined in all the energy ranges by the TB method, with the last paragraph devoted to the analysis of the transport properties when localized defects are present on opposite sides of the QPC. Finally, conclusions and further discussions are given in Sec. V. Appendix A provides some details on the $\mathbf{k} \cdot \mathbf{p}$ method and the analytical approach used for calculations of the transport in the limit of low energy.

II. MODEL

The model Hamiltonian we employ for transition-metal (TM) oxides describes the coupling of the t_{2g} orbitals (d_{xy} , d_{xz} , and d_{yz}) at neighboring Ti lattice sites through the $2p$ orbitals of the oxygen atoms. This TB Hamiltonian turns out to be very accurate for the description of 2D bulk electronic states [10] containing both an atomic spin-orbit coupling and an inversion-symmetry-breaking term [17,23–26]:

$$\mathcal{H} = \sum_{\mathbf{k}} \hat{D}(\mathbf{k})^\dagger H(\mathbf{k}) \hat{D}(\mathbf{k}), \quad (1)$$

with

$$H(\mathbf{k}) = H^0 + H^{\text{SO}} + H^Z + H^M, \quad (2)$$

where $\hat{D}^\dagger(\mathbf{k}) = [c_{yz\uparrow\mathbf{k}}^\dagger, c_{zx\uparrow\mathbf{k}}^\dagger, c_{xy\uparrow\mathbf{k}}^\dagger, c_{yz\downarrow\mathbf{k}}^\dagger, c_{zx\downarrow\mathbf{k}}^\dagger, c_{xy\downarrow\mathbf{k}}^\dagger]$ is a vector whose components are associated with the electron creation operators for a given spin σ ($\sigma = [\uparrow, \downarrow]$), orbital α ($\alpha = [xy, yz, zx]$), and momentum \mathbf{k} in the 2D square Brillouin zone. Then H^0 , H^{SO} , H^Z , and H^M represent the kinetic energy, the spin-orbit, the inversion symmetry breaking and the Zeeman interaction term, respectively.

In the spin-orbital basis, $H_0(\mathbf{k})$ is given by

$$H^0 = \hat{\varepsilon}_{\mathbf{k}} \otimes \hat{\sigma}_0,$$

$$\hat{\varepsilon}_{\mathbf{k}} = \begin{pmatrix} \varepsilon_{yz} & 0 & 0 \\ 0 & \varepsilon_{zx} & 0 \\ 0 & 0 & \varepsilon_{xy} \end{pmatrix},$$

$$\varepsilon_{yz} = 2t_1(1 - \cos k_y a) + 2t_2(1 - \cos k_x a), \quad (3)$$

$$\varepsilon_{zx} = 2t_1(1 - \cos k_x a) + 2t_2(1 - \cos k_y a),$$

$$\varepsilon_{xy} = 4t_1 - 2t_1 \cos k_x a - 2t_1 \cos k_y a + \Delta_t,$$

where $\hat{\sigma}_0$ is the unit matrix in spin space and t_1 and t_2 are the orbital-dependent hopping amplitudes. Δ_t denotes the crystal-field potential as due to the symmetry lowering from cubic to tetragonal also related to inequivalent in-plane and out-of-plane TM-oxygen bond lengths. The symmetry reduction yields a level splitting between the d_{xy} orbital and d_{yz} or d_{zx} orbitals.

H^{SO} denotes the atomic $L \cdot S$ spin-orbit coupling,

$$H^{\text{SO}} = \Delta_{\text{SO}}[\hat{l}_x \otimes \hat{\sigma}_x + \hat{l}_y \otimes \hat{\sigma}_y + \hat{l}_z \otimes \hat{\sigma}_z], \quad (4)$$

with $\hat{\sigma}_i$ ($i = x, y, z$) being the Pauli matrix in spin space and \hat{l}_α ($\alpha = x, y, z$) being the projections of the $L = 2$ angular-momentum operator onto the t_{2g} subspace, i.e.,

$$\hat{l}_x = \begin{pmatrix} 0 & 0 & 0 \\ 0 & 0 & i \\ 0 & -i & 0 \end{pmatrix}, \quad (5)$$

$$\hat{l}_y = \begin{pmatrix} 0 & 0 & -i \\ 0 & 0 & 0 \\ i & 0 & 0 \end{pmatrix}, \quad (6)$$

$$\hat{l}_z = \begin{pmatrix} 0 & i & 0 \\ -i & 0 & 0 \\ 0 & 0 & 0 \end{pmatrix}, \quad (7)$$

assuming $\{d_{yz}, d_{zx}, d_{xy}\}$ as orbital basis.

As mentioned above, the breaking of the mirror plane symmetry, due to the out-of-plane offset of the positions of the TM and oxygen atoms, results into an inversion asymmetric orbital Rashba coupling that is described by the term $H^Z(\mathbf{k})$:

$$H^Z = \gamma[\hat{l}_y \otimes \hat{\sigma}_0 \sin k_x a - \hat{l}_x \otimes \hat{\sigma}_0 \sin k_y a]. \quad (8)$$

This contribution provides an inter-orbital process, due to the broken inversion symmetry, that mixes d_{xy} and d_{yz} or d_{zx} .

Finally, we consider the effects of a magnetic field perpendicular to the plane of the 2DEG. The resulting Zeeman-type interaction is described by the Hamiltonian H^M , which characterizes the coupling of the electron spin and orbital moments to the magnetic field [27]:

$$H^M = M_z[\hat{l}_z \otimes \hat{\sigma}_0 + \hat{l}_0 \otimes \hat{\sigma}_z], \quad (9)$$

with \hat{l}_0 being the unit matrix in the orbital space. We notice that the inclusion of the orbital coupling to the field is only a correction which can be neglected because the spin-orbit coupling is typically larger than the strength of the applied magnetic field considered in the experiment and the Zeeman coupling to the orbital degree of freedom is less relevant. We also neglect the contribution of the vector potential in

the kinetic part of the Hamiltonian. Even though the latter assumption might appear a crude approximation, it can be justified by experimental considerations, which will be detailed below.

The energy separation between adjacent Landau levels can be estimated in terms of the Landé g factor as $\hbar\omega_c = 4/gM_z$, with $g \approx 2$ [27]. For the maximum value of the magnetic energy considered in this work ($M_z = 0.5$ meV), the Landau-level spacing corresponds to 1 meV. On the other hand, the QPC confinement strongly affects the electron mobility μ at the LAO-STO interface [28], which is estimated as $400 \text{ cm}^2 \text{ V}^{-1} \text{ s}^{-1}$ [15]. Accordingly, the corresponding Landau-level broadening is $\hbar e/(m^* \mu) \approx 3.5$ meV, which largely overcomes the level separation. For these reasons, the Landau levels appear to be irrelevant in affecting the transport properties of the system, and thus the kinetic contribution of the vector potential can be safely neglected.

Even enhanced values of the mobility (e. g., $10^3 \text{ cm}^2 \text{ V}^{-1} \text{ s}^{-1}$), corresponding to an energy broadening of 1.4 meV, do not modify the previous conclusion. So far, we have presented arguments based on the assumption that $g \approx 2$. Nevertheless, an enhancement of the g factor could take place in experiments due to the confining effect of the QPC geometry [29]. In the latter case, previous conclusions are even strengthened because, maintaining the same value M_z of the Zeeman splitting, a smaller cyclotron energy is obtained.

In principle, the kinetic contribution of the magnetic field could increase the value of the charge-carrier effective mass [30]. Indeed, the mass renormalization is roughly dependent on the ratio between the cyclotron energy and the mean level spacing induced by the transverse confinement. This estimate leads to a factor $[1 + (\hbar\omega_c)^2 / \langle \Delta E \rangle^2] \approx 1.25$, representing a unimportant mass renormalization not affecting the transport properties.

The electronic structure at the LAO-STO (001) interface has been studied in the literature also within the $\mathbf{k} \cdot \mathbf{p}$ approach [31–33], which is accurate in the limit of large wavelengths. In this paper, we apply the $\mathbf{k} \cdot \mathbf{p}$ procedure directly to the TB Hamiltonian (1). Actually, as discussed in Appendix A, the 2D energy eigenvalues and eigenvectors are exactly determined for small values of the wave vector \mathbf{k} . In particular, in the limit of low energies [23], due to the crystal-field splitting, one can derive an effective spin Rashba interaction α for the xy -like band. Therefore, for small values of the wave vector \mathbf{k} , the d_{xy} -like band is provided by the solutions of the following effective Rashba Hamiltonian H_R :

$$H_R = E_- + \frac{\hbar^2 |\mathbf{k}|^2}{2m_1} + \alpha(\sigma_x k_y - \sigma_y k_x) + M_z \sigma_z, \quad (10)$$

where the energy E_- is

$$E_- = \frac{\Delta_{\text{SO}}}{2} (1 - \epsilon_R - \sqrt{\epsilon_R^2 + 2\epsilon_R + 9}), \quad (11)$$

with $\epsilon_R = |\Delta_t|/\Delta_{\text{SO}}$, m_1 is the lighter mass (smaller than the free electron mass m_e), associated with the higher hopping t_1 ,

$$m_1 = \frac{\hbar^2}{2t_1 a^2} \simeq 0.8m_e, \quad (12)$$

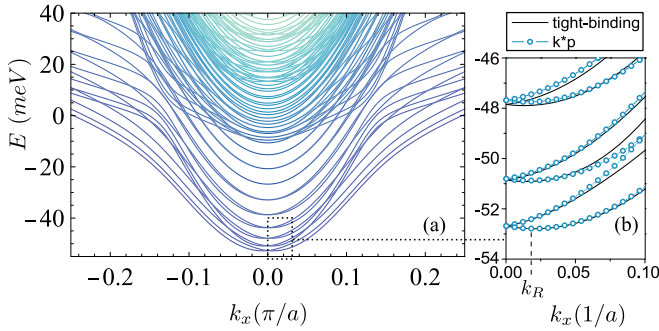


FIG. 2. (a) Band structure for an infinite strip with 64 transverse sites derived from the TB Hamiltonian of Eq. (1). (b) $\mathbf{k} \cdot \mathbf{p}$ approximation for the lowest three sub-bands (blue circles) compared with the tight-binding sub-bands (solid black lines).

and the Rashba coupling constant α is determined as

$$\alpha = \frac{\sqrt{2}a\gamma \exp(\operatorname{arcsinh} \eta_R)}{[1 + \exp(2\operatorname{arcsinh} \eta_R)]}, \quad (13)$$

with

$$\eta_R = \frac{(\epsilon_R + 1)}{2\sqrt{2}}. \quad (14)$$

We remark that, in the literature [17,23,27,33], the typical estimate of the Rashba coupling corresponds to the limit of Eq. (13) for very large ϵ_R :

$$\alpha \simeq \frac{\sqrt{2}a\gamma}{(2\eta_R)} \simeq \frac{2a\gamma \Delta_{SO}}{|\Delta_t|}, \quad (15)$$

which is clearly an overestimation. In any case, the Rashba coupling constant for the xy band depends on the atomic spin-orbit energy Δ_{SO} and the inversion-symmetry-breaking energy γ .

In our work we follow the parameter setting of Ref. [17]: The main hopping $t_1 = 300$ meV, the weaker hopping term $t_2 = 20$ meV, the atomic spin-orbit coupling $\Delta_{SO} = 10$ meV, the orbital Rashba interaction $\gamma = 40$ meV, and the tetragonal crystal field potential $\Delta_t = -50$ meV. Hence, one gets that an estimate of α in Eq. (13) is given by $\alpha \simeq 4.7$ meV nm, a value compatible with experimental measurements [10] in the range of typical 2DEG charge densities. In Appendix A, we show the perfect agreement between the spectrum obtained by the Hamiltonian of Eq. (1) and that from Eq. (10) for small values of the wave vector \mathbf{k} . Moreover, we analyze also the behavior of the spectrum with the inclusion of the effects of the Zeeman energy M_z pointing out that the description provided by the $\mathbf{k} \cdot \mathbf{p}$ procedure is accurate even for large magnetic fields.

Since the QPC investigated in the experiment [15] has a minimal constriction of about 25 nm, we start by analyzing an infinite strip with 64 transverse sites ($64a \simeq 25$ nm, with lattice parameter $a = 0.39$ nm) with hard wall boundary conditions in the transverse direction. As shown in the left panel of Fig. 2, the spectrum is very complex. In fact, since the tetragonal potential $\Delta_t = -50$ meV and the strip is not very narrow, the first sub-bands are derived from the light xy -like bands. Starting from around zero energy, the spectrum is characterized by a large superposition of sub-bands derived not only from the light xy -like bands, but also from the heavy

yz -like and zx -like bands. Therefore, at high energies, the spectrum shows a quasicontinuum, while, at low energies, the xy -like sub-bands are quite distinct. Moreover, we point out that, in the left panel of Fig. 2, the first three xy -like sub-bands show a clear double minimum close to $\mathbf{k} = 0$, an effect that can be typically ascribed to the Rashba coupling in Rashba nanowires [34–39]. However, for the next xy -like sub-bands, the double-minimum gets reduced with increasing energy. Moreover, the separation between the minima of first sub-bands follows the behavior expected for nanowires with hard wall conditions, while the next xy -like bands show even a reduction in the energy difference between the minima. These effects are obviously enhanced close to the onset of the quasicontinuum due to the contribution of heavy yz - and zx -like bands. Actually, the multi-orbital character of the problem is able to provide a complex behavior even in the case of the infinite strip.

We notice that the sub-band occupation in the experiment [15] corresponds only to the first three xy -like ones. Actually, the range of the charge densities considered in this experiment is below 10^{13} cm $^{-2}$. Therefore, as discussed in Appendix A, we adopt a $\mathbf{k} \cdot \mathbf{p}$ procedure to analyze the properties of the first xy -like sub-bands in the strip setting up the Hamiltonian H_S derived from Eq. (10):

$$H_S = E_- + \frac{(\hbar^2 k_x^2 + p_y^2)}{2m_1} + \alpha \left(\sigma_x \frac{p_y}{\hbar} - \sigma_y k_x \right) + M_z \sigma_z + V(y), \quad (16)$$

where $p_y = -i\hbar d/dy$ is the momentum operator along the y direction, and $V(y)$ imposes hard wall conditions on the transverse boundary along y (lateral size equal to $64a$). We explicitly fix the parameters E_- , m_1 , and α as derived from the 2D bulk. As discussed in Appendix A, the exact solution of H_S can be obtained analytically for small values of \mathbf{k} . Particularly interesting are the effects due to the spin-orbit Rashba coupling which can be quantified through the wave vector $k_R = m_1 \alpha / \hbar^2$. In fact, the single-particle spectrum of the xy -like sub-bands not only shows minima centered at $\pm k_R$, but it is globally reduced of the energy $\hbar^2 k_R^2 / 2m_1$. In the next section, we discuss how these effects determine the behavior of the conductance as a function of the gate voltage V_G and the bias voltage V_B . As shown in the right panel of Fig. 2, the results of the $\mathbf{k} \cdot \mathbf{p}$ approximation are able to provide an accurate description for the lowest three xy -like sub-bands for small values of k_x . Tiny deviations from the TB scheme are present only for the third sub-band. We stress that the $\mathbf{k} \cdot \mathbf{p}$ approximation captures the correct position of the minima of the sub-bands, therefore, as shown in the next section, it will provide a simplified but accurate model for the transport through the adiabatic QPC.

III. LOW-ENERGY TRANSPORT

In this section, we discuss the low-energy transport in order to analyze and clarify some aspects of recent experimental data given in Ref. [15]. As discussed in previous sections, within this experimental setup, only the first three xy -like sub-bands are occupied by charge carriers which cross the QPC with 25 nm minimal constriction and a smooth curvature. Therefore, in this section, we adopt the adiabatic

approximation, briefly discussed in Appendix A, for the treatment of the transport [1,2,40]. We remark that all the results discussed in this section have been confirmed by analogous simulations done with the more realistic TB scheme which will be exposed in the next section. Indeed, the scheme used in this section provides transport properties in the energy range of the first two sub-bands which are in very good agreement with the TB method.

As discussed in Appendix A, for the description of the QPC, we adopt the Hamiltonian H_Q derived from Eq. (10):

$$H_Q = E_- + \frac{(p_x^2 + p_y^2)}{2m_1} + \frac{\alpha}{\hbar}(\sigma_x p_y - \sigma_y p_x) + M_z \sigma_z + V(x, y), \quad (17)$$

where $p_x = -i\hbar d/dx$ and $p_y = -i\hbar d/dy$ are the momentum operators along the x and y directions, respectively, and the potential $V(x, y)$ imposes hard wall conditions on the x -dependent transverse boundary determined by $W(x)/2$ and $-W(x)/2$ [41]. Clearly, according to the experimental setup of Ref. [15], $W(0) = 64a$ and $W(x) = W(0) + \beta x^2$, with $\beta \simeq 0.01 \text{ nm}^{-1}$, that is the curvature of the QPC is small.

For small values of the parameter β , the adiabatic approximation [42] can be implemented for the treatment of Hamiltonian (17). As discussed in Appendix A, at first, the eigenvalue problem is solved in the “fast” variable y considering the “slow” variable x as fixed, then the resulting equation in the slow variable x is considered. Actually, this procedure can be analytically implemented not only in the presence of Rashba spin-orbit coupling, but also in the presence of an out-of-plane magnetic field. As a result, the effects of the small curvature can be quantified for the QPC. Indeed, as detailed in Appendix A, within the adiabatic approximation, for the slow variable x , one gets the potential of an inverted harmonic oscillator whose angular frequency $\omega_n = n\omega_1$ depends on the sub-band label n . The frequency ω_1 depends on the square root of β . For $\beta = 0.01 \text{ nm}^{-1}$, $\hbar\omega_1 \simeq 0.26 \text{ meV}$, which is much smaller than all the energy differences between sub-bands considered in this work. Therefore, for the first sub-bands, the adiabatic approximation can be used to accurately predict the transport properties. The main effect of the finite small curvature is to slightly smooth the conductance steps of the conductance even at very low temperatures. We remark that the rounding of the conductance steps is present in the experimental data of Ref. [15], which we thoroughly discuss below.

As discussed in Appendix A, we analytically calculated the current I as a function of the gate voltage V_G and the bias voltage V_B in the presence of an applied magnetic field normal to the interface. Since many experiments show that the Rashba coupling constant α can change with varying the gate voltage V_G [10,11], we consider three different values for this parameter: $\alpha = 0$, $\alpha = 2 \text{ meV nm}$, which should correspond to a minimum at the LAO-STO interface, for charge densities less than 10^{13} cm^{-2} , and $\alpha = 4 \text{ meV nm}$, which is slightly smaller than the value corresponding to typical 2DEG electron densities [9]. We discuss transport properties both in the absence and in the presence of an applied magnetic field.

First, we discuss the effects of the spin-orbit Rashba coupling α on the behavior of the conductance G (defined as $\partial I/\partial V_B$ in the limit $V_B \rightarrow 0^+$) as a function of the gate

potential V_G . As reported in the left panel of Fig. 3, the conductance shows plateaus corresponding to quantized values of the conductance quantum $G_0 = 2e^2/h$ in agreement with experimental results [15] which indicate a ballistic transport in the QPC. From the comparison with low-energy bands in Fig. 2, we notice that the onset of the plateaus does not precisely coincide with the minima of the bands. Actually, as discussed in Appendix A, the smoothing of the step between two consecutive plateaus is due to the small but finite spatial curvature of the adiabatic QPC shown in Fig. 1. We remark that the value of the curvature is extracted from the experimental setup in Ref. [15], and that the Rashba coupling provides a small but finite shift of the conductance curves, in agreement with the effects discussed in Fig. 2 about the energy spectrum. Additional effects are not expected in the low-energy regime since the Rashba term is proportional to the momentum operator and therefore to the first derivative of the wave function which is slowly changing in the adiabatic QPC with increasing the coordinate x . In the next section, however, we will find that effects due to the atomic spin-orbit and the inversion-symmetry-breaking term get enhanced with increasing energy range.

For the discussion of the differential conductance and the transconductance in the absence of magnetic field, we consider a Rashba coupling constant $\alpha = 2 \text{ meV nm}$, since it is close to experimental estimates in the limit of low charge density. In the middle panel of Fig. 3, we plot the differential conductance (defined as the derivative of the current with respect to V_B) as a function of bias potential V_B for several values of the split-gate potential. The differential conductance presents plateaus not only at nG_0 but also at $(n + 1/2)G_0$. Actually, additional plateaus at $(n + 1/2)G_0$ can be obtained when the number of modes available for left-going and right-going charge carriers differs by one [43–45]. This effect takes place when the energy eV_B exceeds the splitting between two sub-bands. Moreover, in our 2D model, at odds with experimental results, we find a perfect symmetry between positive and negative values of bias potential V_B .

In the right panel of Fig. 3, we show contour plots of the transconductance $\partial^2 I/\partial V_G \partial V_B$ as a function of bias potential V_B and gate potential V_G in the absence of magnetic field. Therefore, we analyze again the nonlinear transport, emphasizing now the transitions between the conductance plateaus. The maxima of the transconductance form a diamond-like structure centered at $V_B = 0$. Apparently, the maxima decrease with increasing energy, while, at the same time, the diamond-like structure gets enlarged. Therefore, the edges of the diamonds provide directly the separation between two consecutive energy levels. We point out that the results for the differential conductance and the transconductance are in good agreement with experiment [15] in the absence of magnetic field.

We investigate now the effects of a magnetic field perpendicular to the 2-DEG plane on the transport properties. As seen in the left panel of Fig. 4, the plateaus of conductance are quantized in half-integer values of G_0 , indicating that the spin degeneracy is lifted. In analogy with Fig. 4, we first analyze the effects of three different values of Rashba coupling, then we consider $\alpha = 2.0 \text{ meV nm}$ for the study of further transport properties. In particular, in the middle panel

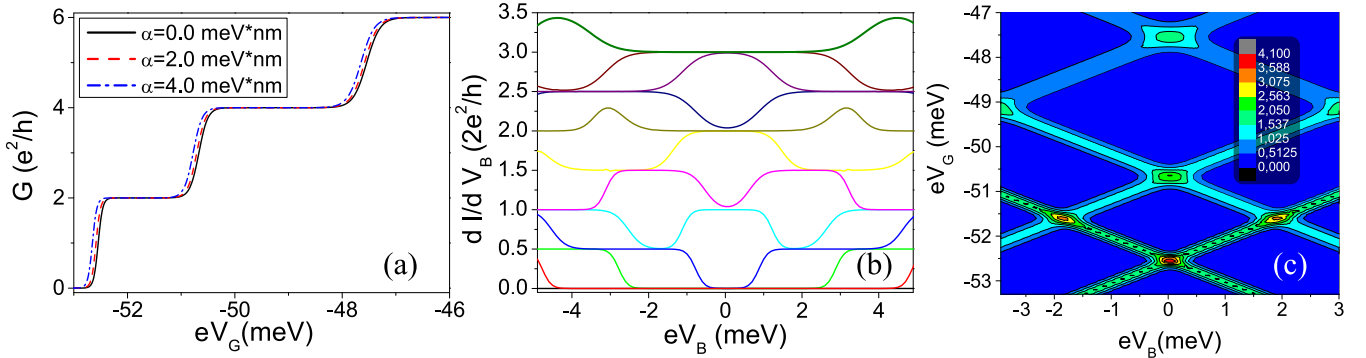


FIG. 3. QPC in the presence of Rashba coupling. (a) Conductance G of the QPC as a function of gate voltage V_G for three different values of the Rashba coupling constant α . (b) Differential conductance as a function of bias potential V_B for several values of the split-gate potential at Rashba coupling constant $\alpha = 2$ meV nm: Colored curves correspond to values of eV_G from -55 to -45 meV through steps of 1 meV. (c) Map of transconductance as a function of V_G and V_B at Rashba coupling constant $\alpha = 2$ meV nm.

of Fig. 4, we plot the conductance G for several values of the magnetic energy M_z focusing on the halving of the step. Apparently, the additional plateau at half G_0 gets enhanced with increasing strength of the magnetic field. Finally, in the right panel of Fig. 4, we show contour plots of the transconductance as a function of V_G and V_B in the presence of the magnetic field. Seemingly, making the comparison with the right panel of Fig. 4, the magnetic field involves a duplication of the diamond-like structure. We remark that most features of the conductance and the transconductance are in good agreement with experimental results [15] even in the presence of a magnetic field.

IV. MULTI-ORBITAL TRANSPORT

In this section we describe the electronic transport properties of the QPC within the TB approximation by numerically implementing a finite-size system described by the Hamiltonian (1). This description allows us to go beyond the low-energy regime, which has been significantly characterized by the $\mathbf{k} \cdot \mathbf{p}$ method. We show that the TB approach is necessary to get insights on the multi-orbital ballistic transport characteristic of higher doping densities. The conductance of the QPC, which is schematized in Fig. 1, is calculated within

the TB method by using the KWANT [46] and NUMPY [47] libraries.

By looking at Fig. 5(a) we see that, while the atomic spin-orbit term mainly introduces an orbital-dependent energy shift, the orbital Rashba coupling, weighted by γ , acts more intriguingly: Low-energy subbands are left unchanged while high-energy ones are squeezed toward negative energies. The width of the plateaus is almost constant or decreasing, while it should be expected to be linearly increasing because of the hard wall confinement in the transverse direction. Indeed, it is possible to see in Fig. 2 that the distance between the lowest type of sub-bands (related to the orbital d_{xy}) is not increasing. Therefore, hybridization at higher energy between sub-bands with similar orbital character is able to change the energy spectrum and the conductance of the adiabatic QPC. Finally, we notice that, at higher charge densities, where the hybridization takes place between all three orbitals, the plateaus are very narrow. At the highest densities considered in this paper, the plateaus completely disappear, so that the conductance curve does not show any quantization. In fact, as seen in Fig. 2, the yz - and zx -like sub-bands are heavier than the xy -like sub-bands, therefore, they gather more easily at energies of the order of 0–40 meV, creating a quasicontinuum.

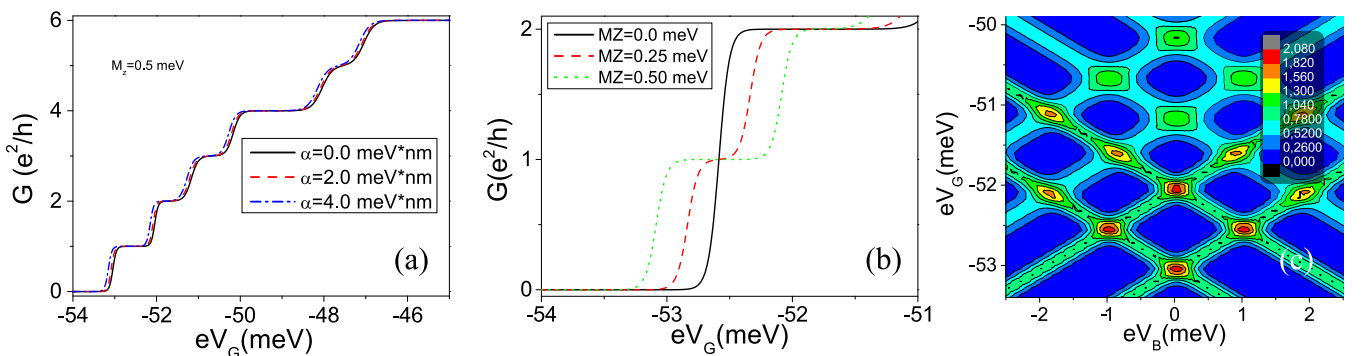


FIG. 4. QPC in the presence of Rashba coupling and out-of-plane magnetic field. (a) Conductance G as a function of gate potential V_G for three different values of Rashba coupling constant α at magnetic energy $M_z = 0.5$ meV. (b) Conductance G as a function of gate potential V_G for several values of the magnetic energy M_z at a Rashba coupling $\alpha = 2.0$ meV nm. (c) Map of transconductance as a function of V_G and V_B at magnetic energy $M_z = 0.5$ meV at a Rashba coupling $\alpha = 2.0$ meV nm.

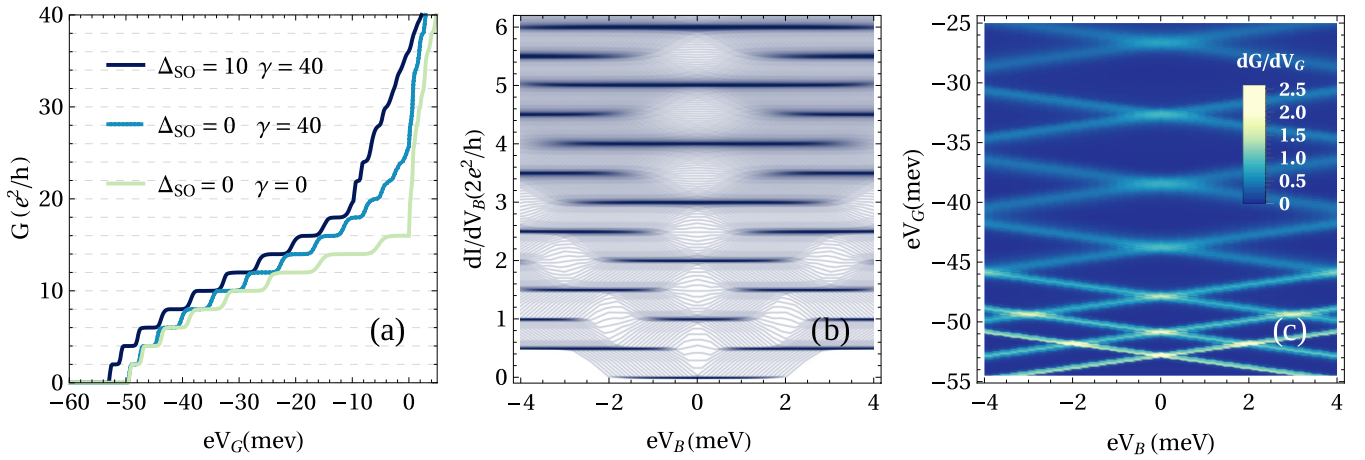


FIG. 5. (a) Conductance of the QPC as a function of energy for three different set of Hamiltonian parameters, as indicated in the legend. (b) Differential conductance as a function of V_B for several values of the split-gate potential. (c) Map of the transconductance as a function of V_G and V_B .

In analogy with the results reported in Fig. 4, Figs. 5(b) and 5(c) show the differential conductance and the map of the transconductance. The differential conductance presents plateaus at nG_0 and $(n + 1/2)G_0$ in a large range of energies. Furthermore, the symmetry between positive and negative values of bias potential V_B is kept for all the sub-bands analyzed in the paper. Likewise, the transconductance shows maxima forming a diamond-like structure centered at $V_B = 0$ up to large energies. The diamonds are visible up to energies of the order of -25 meV, hence well beyond the range of energies studied in the previous section. Indeed, some features of the nonlinear transport are similar to those found in the low-energy limit. However, both pictures emphasize the nonincreasing energy distance between sub-bands determined by the orbital Rashba coupling γ .

Finally, we analyze the effects of the magnetic field on the linear and nonlinear transport properties in the energy range where xy -like sub-bands provide the relevant spectrum. Quite surprisingly, the effect of the turning-on of an out-of-plane magnetic field is only visible for low energies. Indeed, in complete analogy with the results discussed in the previous section, we see in Fig. 6(a) that the expected halving of

plateaus occurs only for the first two or three sub-bands. On the other hand, higher-energy plateaus are only smoothed, as visible also from the differential conductance in Fig. 6(b) and the transconductance in 6(c). We stress that this effect is due to the strong interplay between the orbital Rashba coupling γ , the atomic spin-orbit energy Δ_{SO} and the Zeeman term M_Z . In fact, with increasing energy, the splittings induced by the magnetic field are quenched, therefore the sub-band spectrum is strongly affected by other energy terms mixing different sub-bands and orbitals.

Effects of localized defects on the conductance. In this paragraph, we provide a possible explanation for the oscillations of the conductance observed in the experiment of Jouan *et al.* [15]. Although the oscillation could be due to different experimental motivations, here we try to understand if the existence of such oscillations can be ascribed to the presence of specific “defects.” In particular, we focus on the presence of localized defects present on opposite sides of the QPC (see Fig. 7). Indeed, we show that defects can induce conductance oscillations whose amplitude gets enhanced with increasing energy.

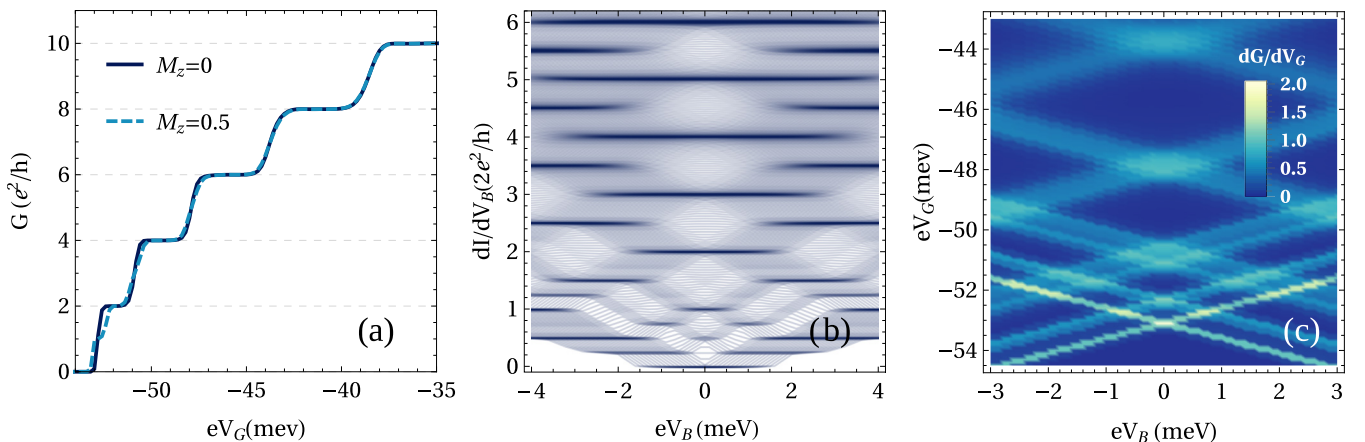


FIG. 6. (a) Conductance of the QPC as a function of energy in presence of an out-of-plane magnetic field. (b) Differential conductance as a function of V_B for several values of the split-gate potential at the magnetic energy $M_z = 0.5$ meV. (c) Map of transconductance as a function of V_G and V_B at the magnetic energy $M_z = 0.5$ meV.

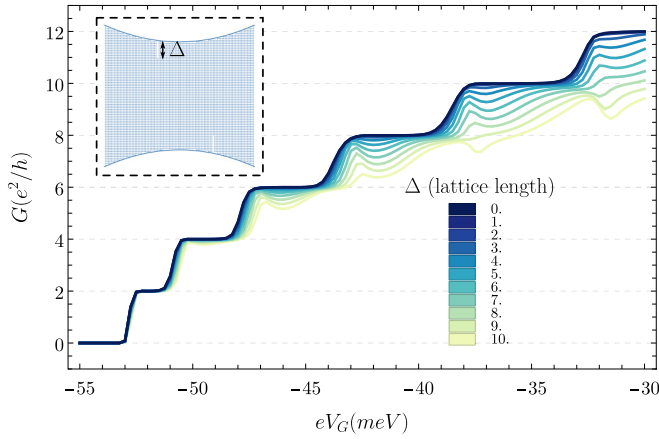


FIG. 7. Conductance G of the QPC as a function of the gate potential V_G for different lengths Δ of the holes on the two sides of the QPC. In the inset the position of the two defects, one on top side of the QPC, the other on the down side.

First, we have considered the effect of an extended spatial modulation on the border of the QPC. We have found that this perturbation is not able to strongly affect the conductance. Next, we have examined the effects of two localized defects close to opposite borders of the QPC as shown in the inset of Fig. 7: Two pin-like irregularities with variable depth Δ . In fact, the couple of defects induces a progressive reduction of the value of the conductance at the plateaus with increasing the energy. Moreover, as seen in Fig. 7, this value of the conductance gets lowered with increasing length of the defect. Finally, this reduction is accompanied also by numerous oscillations of the conductance. We have checked that neither the atomic spin-orbit coupling nor the asymmetric Rashba coupling are able to hamper the decreasing value of the conductance and its oscillating behavior, which can be entirely ascribed to interference effects between the two holes. Moreover, we have investigated the behavior of the conductance as a function of the distance between the two localized defects (Fig. 8). The analysis shows oscillations related to

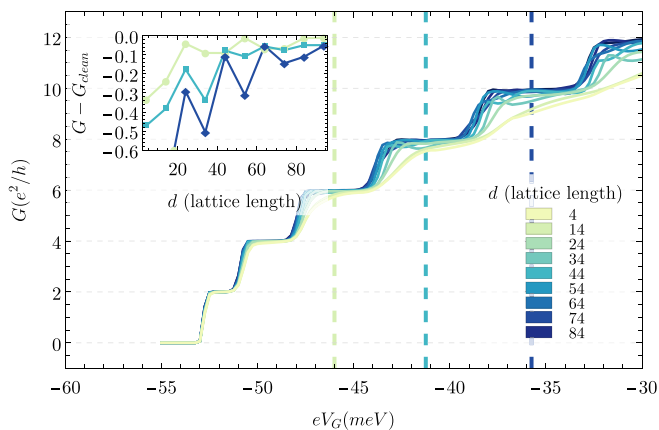


FIG. 8. Conductance G of the QPC as a function of the gate potential V_G for different distances d between the two defects. In the inset, the variation of the conductance due to the defects as a function of the distance between the two defects, for three different values of the gate potential V_G , as indicated in the main plot.

a Fabry-Perot-like interference effect, in which one expects a maximum of the conductance when the distance between the two defects matches the electron wavelength with even multiples. However the multi-orbital character of the considered Hamiltonian does not allow a quantitative description of this phenomenon. This paragraph completes our work which hence provides a comprehensive description of the ballistic transport in several regimes.

V. CONCLUSIONS AND DISCUSSIONS

In this paper, we have analyzed linear and nonlinear ballistic transport properties within the Landauer-Büttiker method using the TB model and the $\mathbf{k} \cdot \mathbf{p}$ approach for the electronic structure of an adiabatic QPC at the (001) LAO-STO interface in the nonsuperconducting state. We have focused on the interplay between the atomic spin-orbit coupling, the inversion-symmetry-breaking term, and the out-of-plane magnetic field pointing out three transport regimes. The first one takes into account the first xy -like sub-bands, therefore it is limited to low energies. In this regime, the quantization of the conductance is quite marked both in the absence and presence of the magnetic field. The second transport regime is found at intermediate energies, since it involves further d_{xy} -like sub-bands. In this regime, the conductance quantization is less pronounced since typical strengths of the magnetic field are not able to induce the splitting of the sub-bands hindering the increase of transport channels. Moreover, due to the orbital Rashba coupling γ , the energy distance between sub-bands does not increase with increasing energy at odds with what occurs for the first xy -subbands. Finally, the third transport regime is characterized by the mixing between light d_{xy} -like and heavy d_{yz} -like, d_{zx} -like sub-bands so that the conductance plateaus become very narrow, indicating that the conductance quantization is weak.

This work has been partly motivated by recent experiments [15] exploring low-energy transport in the normal state. In particular, in experimental data, oscillations of the conductance can be observed on the plateaus. To address this issue, we have analyzed the effects of localized pin-like defects present on external sides of the QPC. Indeed, it is found that localized defects are able to induce conductance oscillations whose amplitude gets enhanced with increasing energy. As a result of our analysis, these oscillations can be ascribed to interference effects associated with the geometry of the constriction.

In this paper, the focus has been on the transport properties of the normal state. Therefore, this work represents only the starting point for the theoretical analysis of superconducting QPCs which can be very relevant for addressing the possibility of topological superconductivity and Majorana fermions [48] at the LAO-STO interface [17,18,49]. Work in this direction is in progress.

ACKNOWLEDGMENTS

We acknowledge useful discussions with Mario Cuoco, Fiona Forte, and Marco Salluzzo. This work was supported by the project Quantox Grant Agreement No. 731473,

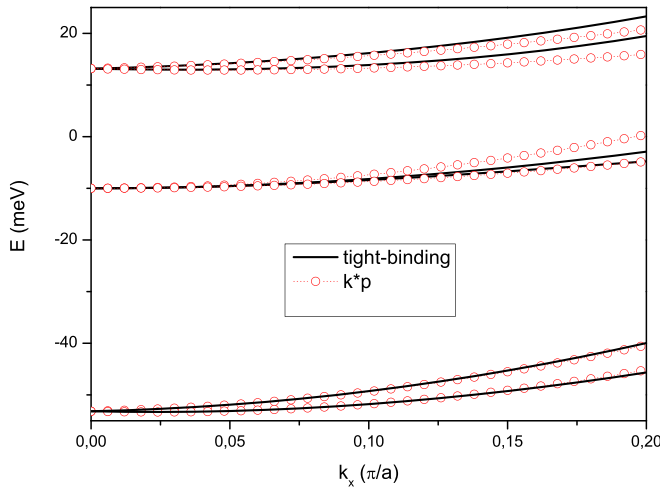


FIG. 9. 2D bulk energy eigenvalues (in units of meV) as a function of the wave vector k_x (in units of π/a): Comparison between the results in the $\mathbf{k} \cdot \mathbf{p}$ and the TB method.

QuantERA-NET Cofund in Quantum Technologies implemented within the EU-H2020 Programme, and the project Two-dimensional Oxides Platform for SPIN-orbitronics nanotechnology (TOPSPIN), funded by the MIUR-PRIN Bando 2017 - Grant No. 20177SL7HC.

APPENDIX A: METHODS FOR CONTINUUM MODELS

In this Appendix we briefly discuss the $\mathbf{k} \cdot \mathbf{p}$ approach used for analytical calculations of the electronic structure of the 2D bulk, the strip and the QPC. Finally, we provide some details on the calculation of the conductance of the adiabatic QPC starting from the $\mathbf{k} \cdot \mathbf{p}$ energy levels.

1. $\mathbf{k} \cdot \mathbf{p}$ method for two-dimensional bulk

In this section, we apply the $\mathbf{k} \cdot \mathbf{p}$ procedure directly to the TB 2D Hamiltonian in Eq. (1) getting energy eigenvalues and eigenvectors which are exact for small values of the wave vector \mathbf{k} . In particular, at $\mathbf{k} = 0$, the inversion-symmetry-breaking term (8) vanishes, therefore the TB Hamiltonian can be analytically diagonalized, providing, in the case of zero magnetic field, the eigenvalues E_{\pm} :

$$E_{\pm} = \frac{\Delta_{SO}}{2} (1 - \epsilon_R \pm \sqrt{\epsilon_R^2 + 2\epsilon_R + 9}), \quad (\text{A1})$$

with $\epsilon_R = |\Delta_t|/\Delta_{SO}$, and the eigenvalue $E_0 = -\Delta_{SO}$. Then, one considers the matrix elements of the \mathbf{k} -dependent inversion-symmetry-breaking term and the kinetic energy between the exact eigenstates obtained at $\mathbf{k} = 0$ finding approximate eigenvalues at finite \mathbf{k} .

We recall that, in this paper, the following parameters are used for the 2DEG at LAO-STO (001) interface [17] with typical carrier densities: $t_1 = 300$ meV, $t_2 = 20$ meV, $\Delta_{SO} = 10$ meV, $\gamma = 40$ meV, $\Delta_t = -50$ meV. Therefore, as shown in Fig. 9, at $\mathbf{k} = 0$, one gets three eigenvalues which are doubly degenerate. Then, the degeneracy is broken at finite \mathbf{k} . In particular, we point out the different behavior as a function of $\mathbf{k} = 0$ for the first xy -like and the third zx -like doublet. This behavior indicates the possibility to describe the spectrum in

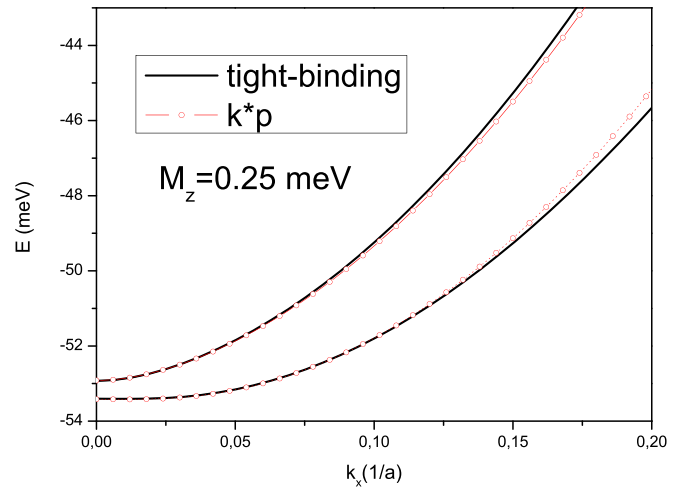


FIG. 10. 2D strip low-energy eigenvalues (in units of meV) as a function of the wave vector k_x (in units of π/a) for magnetic energy $M_z = 0.25$ meV: Comparison between the results in the $\mathbf{k} \cdot \mathbf{p}$ and the TB method.

terms of an emergent Rashba coupling constant α , which, for the first doublet, has been specified in previous sections of the paper. For the first xy -like doublet, the term quadratic in the wave vector depends on the mass m_1 defined in Eq. (12). On the other hand, the second doublet corresponding to yz -like bands starts at the atomic energy E_0 and cannot be interpreted in terms of a Rashba term linear in the wave vector [17].

Finally, we use the $\mathbf{k} \cdot \mathbf{p}$ method to get the 2D band structure in the presence of an out-of-plane magnetic field. Seemingly, the method is able to grasp the gap at $\mathbf{k} = 0$ induced by the applied magnetic field and provide the bands at finite but small values of the wave vector.

2. $\mathbf{k} \cdot \mathbf{p}$ method for strip

We adopt the $\mathbf{k} \cdot \mathbf{p}$ procedure to analyze the properties of the first xy -like sub-bands in the strip. Toward this end, we explicitly consider the parameters E_- , m_1 , and α as derived from $\mathbf{k} \cdot \mathbf{p}$ procedure in the 2D bulk. Once these parameters are fixed, the corresponding Hamiltonian for the strip given in Eq. (16) can be solved exactly at $k_x = 0$ and complex matrix elements of the Hamiltonian operator (at small k_x) between the eigenvectors at $k_x = 0$ can be evaluated analytically. This procedure provides an accurate description for the lowest three xy -like sub-bands for small values of k_x [Fig. 1(b)]. In Fig. 10 we compare the $\mathbf{k} \cdot \mathbf{p}$ approximation for the lowest bands of the strip with the TB one in presence of a magnetic field.

3. Adiabatic approximation for the quantum point contact

As before, we explicitly consider the parameters E_- , m_1 , and α as derived from $\mathbf{k} \cdot \mathbf{p}$ procedure in the 2D bulk. Therefore, we use the $\mathbf{k} \cdot \mathbf{p}$ procedure to set up the Hamiltonian given in Eq. (17), which is solved by exploiting the small curvature of the QPC. Hard wall conditions imposed by the potential $V(x, y)$ on the x -dependent transverse boundary are determined by $W(x)/2$ and $-W(x)/2$, where $W(x) = W(0) + \beta x^2$, with $W(0) = 64a$ and $\beta \simeq 0.01$ nm $^{-1}$, which represents

the small parameter at the basis of the adiabatic procedure. We will provide details of the adiabatic approximation including the effects of the spin-orbit Rashba coupling. The procedure in the presence of the out-of-plane magnetic field can be easily generalized since the typical strengths of the magnetic fields mainly affect the sub-bands already split by the spin-orbit coupling.

At first, the eigenvalue problem is solved in the fast variable y , considering the slow variable x as fixed. The adiabatic approximation is implemented for the treatment of Hamiltonian (17) including the spin-orbit coupling, therefore one starts from the following eigenvalue problem with $M_z = 0$:

$$h_0(x, y)\chi_{n,\beta}(x, y) = E_n(x)\chi_{n,\beta}(x, y), \quad (\text{A2})$$

where $\chi_{n,\beta}(x, y)$ is the spinor corresponding to the twofold degenerate x -dependent energy level $E_n(x)$ eigenvalue, with n sub-band labels and $\beta = 1, 2$, labels of the eigenfunction. Moreover, the operator $h_0(x, y)$ is

$$h_0(x, y) = \frac{p_y^2}{2m_1} + \frac{\alpha}{\hbar}\sigma_x p_y + V(x, y), \quad (\text{A3})$$

with $p_y = -i\hbar d/dy$ being the momentum operator along the y direction, and x treated as a parameter. This problem is exactly solved [34], providing the following expression for the energy level $E_n(x)$:

$$E_n(x) = E_- + \frac{\hbar^2}{2m_1} \left[\frac{n^2\pi^2}{W(x)^2} - k_R^2 \right], \quad (\text{A4})$$

with k_R being the spin-orbit Rashba wave vector.

To solve the full Hamiltonian (17), one chooses its eigenvector $\Psi(x, y)$ corresponding to the eigenvalue E as

$$\Psi(x, y) = \sum_{n,\beta} \phi_{n,\beta}(x)\chi_{n,\beta}(x, y), \quad (\text{A5})$$

where the spinor $\chi_{n,\beta}(x, y)$ solves the eigenvalue problem given by $h_0(x, y)$ in Eq. (A3). Therefore, exploiting the adiabatic regime, one can neglect the derivative of $\chi_{n,\beta}(x, y)$ with respect to the slow variable x , obtaining the following equations for the functions $\phi_{n,\beta}(x)$ at the energy $E = E_n$ relative to each sub-band n :

$$\begin{aligned} \left[\frac{p_x^2}{2m_1} + E_n(x) \right] \phi_{n,1}(x) - \frac{\alpha}{\hbar} A_{1,2}^n(x) p_x \phi_{n,2}(x) &= E_n \phi_{n,1}(x), \\ \left[\frac{p_x^2}{2m_1} + E_n(x) \right] \phi_{n,2}(x) - \frac{\alpha}{\hbar} A_{2,1}^n(x) p_x \phi_{n,1}(x) &= E_n \phi_{n,2}(x), \end{aligned} \quad (\text{A6})$$

where the matrix elements $A_{\beta,\gamma}^n$ are defined as

$$A_{\beta,\gamma}^n(x) = \int_{-W(x)/2}^{W(x)/2} \chi_{n,\beta}^*(x, y) \sigma_y \chi_{n,\gamma}(x, y), \quad (\text{A7})$$

with σ_y being the Pauli matrix relative to the y spin component. We point out that $A_{1,1}^n(x) = A_{2,2}^n(x) = 0$ and $A_{2,1}^n(x) = -A_{1,2}^n(x)$. Actually, as expected within the adiabatic approach, the energy $E_n(x)$ plays the role of the potential for the slow variable x . In the limit of a small curvature for the QPC, one can consider the lowest-order expansion for the quantities

$E_n(x)$ and $A_{1,2}^n(x)$, getting

$$E_n(x) \simeq E_{n0} - \frac{1}{2}m_1\omega_n^2x^2, \quad (\text{A8})$$

with

$$E_{n0} = E_- + \frac{\hbar^2}{2m_1} \left[\frac{n^2\pi^2}{W(0)^2} - k_R^2 \right], \quad (\text{A9})$$

and ω_n determined by the second derivative $W_0'' = 2\beta$ of the function $W(x)$ at the center point $x = 0$ of the QPC,

$$\omega_n = n \sqrt{\frac{\hbar^2\pi^2W_0''}{2m_1^2W(0)^3}}, \quad (\text{A10})$$

and $A_{1,2}^n(x) \simeq A_{1,2}^n(0) = -iK_{n0}$, with

$$K_{n0} = \frac{\sin[k_R W(0)]}{k_R W(0)} \frac{n^2\pi^2}{[n^2\pi^2 - k_R^2 W(0)^2]}. \quad (\text{A11})$$

Even for $n = 1$, the values of the Rashba spin-orbit coupling are not so large that the denominator of Eq. (A11) does not vanish.

The coupled equations for the functions $\phi_{n,\beta}(x)$ relative to sub-band n can be recast for the rotated functions $\delta_{n,\beta}$ in the same following equation:

$$\left[\frac{p_x^2}{2m_1} + \tilde{E}_{n0} - \frac{1}{2}m_1\omega_n^2x^2 \right] \delta_{n,\beta}(x) = E_n \delta_{n,\beta}(x), \quad (\text{A12})$$

where \tilde{E}_{n0} is defined as

$$\tilde{E}_{n0} = E_{n0} - \frac{\hbar^2 k_R^2}{2m_1} K_{n0}^2, \quad (\text{A13})$$

with E_{n0} given in Eq. (A9) and K_{n0} in Eq. (A11). As discussed in the main text, the Rashba spin-orbit coupling provides not only a small rigid shift for all the sub-bands but also weak corrections dependent on the sub-band level. Both corrections are quadratic in the Rashba wave vector k_R .

Once the energy levels \tilde{E}_{n0} and the level-dependent quantities ω_n are known, using the Landauer-Büttiker approach [2,40], the contribution of each channel to the conductance of the QPC is given by its transmission T_n :

$$T_n(E) = \frac{1}{1 + \exp(-\pi\epsilon_n)}, \quad (\text{A14})$$

where $\epsilon_n = 2(E - \tilde{E}_{n0})/\hbar\omega_n$. The total transmission is the sum of the transmission of each of the channels. Therefore, the quantities ω_n provide a smoothing of the transmission steps depending on the curvature of the QPC. Finally, from the transmission, we have calculated the current I as a function of the gate voltage V_G and the bias voltage V_B in the presence of an applied magnetic field normal to the interface.

In Fig. 11, we compare the conductance of the QPC calculated within the continuum model in the absence of the magnetic field with that evaluated numerically within the one-band Rashba spin-orbit TB model. Actually, in 2D, this TB model represents the discretized version of the 2D continuum model used for the analytical calculation of the conductance and it has been investigated in the past for clarifying the effects of Rashba spin-orbit coupling in different transport regimes [50]. In any case, the calculation of the conductance within the TB model is performed in a way similar to what

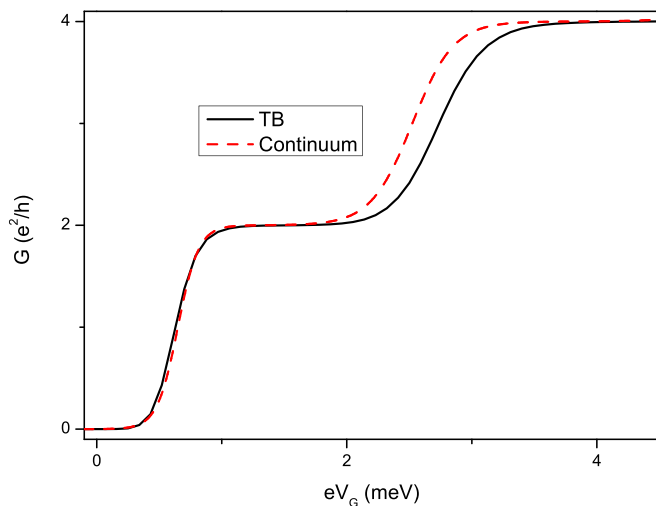


FIG. 11. Conductance (in units of e^2/h as a function of the gate energy in meV) for the TB model (solid black line) and the continuum model of the QPC (red dashed line) at finite values of Rashba spin-orbit coupling.

is done in the literature [50]. The energies have been shifted by $-E_-$, so that the minimum of the 2D electronic bands is at zero energy for both the continuum and TB models. As discussed in the main text, the conductance due to the first two sub-bands is accurately described by the continuum model. Only the conduction from the second sub-band starts from energies slightly smaller than those predicted by the TB

approach. This is an effect of the curvature of the QPC since, in the continuum model, we have explicitly used the expansion in terms of low curvature, which is an approximation that is not exploited within the numerical TB scheme.

APPENDIX B: DIFFERENTIAL CONDUCTANCE AND TRANSCONDUCTANCE

The current at finite bias is calculated as

$$I(eV_G, eV_B) = \frac{e}{h} \sum_n \int_{-\infty}^{\infty} T_n(E) [f_L(E) - f_R(E)] dE, \quad (\text{B1})$$

where

$$f_{L,R}(E) = f_0(E \mp eV_B/2), \quad (\text{B2})$$

and $f_0(E)$ is the Fermi-Dirac distribution calculated with $\mu = eV_G$,

$$f_0(E) = \frac{1}{1 + e^{(E - eV_G)/(k_B T)}}. \quad (\text{B3})$$

$T_n(E)$ are evaluated as in Eq. (A14) for the low-energy transport and via the tight-binding scattering matrix by using the KWANT [46] and NUMPY [47] libraries for the multi-orbital transport. The differential conductance is then evaluated as $\frac{dI}{dV_B}$, and the transconductance is evaluated as $\frac{d^2I}{dV_G dV_B}$. The usual conductance G is the limit of $\frac{dI}{dV_B}$ for $V_B \rightarrow 0$, which at zero temperature reduces to $G(eV_G) = \frac{e^2}{h} \sum_n T_n(eV_G)$.

-
- [1] B. J. van Wees, H. van Houten, C. W. J. Beenakker, J. G. Williamson, L. P. Kouwenhoven, D. van der Marel, and C. T. Foxon, *Phys. Rev. Lett.* **60**, 848 (1988).
- [2] M. Büttiker, *Phys. Rev. B* **41**, 7906(R) (1990).
- [3] R. Landauer, *Z. Phys. B: Condens. Matter* **68**, 217 (1987).
- [4] B. J. van Wees, L. P. Kouwenhoven, H. van Houten, C. W. J. Beenakker, J. E. Mooij, C. T. Foxon, and J. J. Harris, *Phys. Rev. B* **38**, 3625 (1988).
- [5] C. Rossler, S. Baer, E. de Wiljes, P.-L. Ardelit, T. Ihn, K. Ensslin, C. Reichl, and W. Wegscheider, *New J. Phys.* **13**, 113006 (2011).
- [6] S. B. Ogale, in *Thin Films and Heterostructures for Oxide Electronics*, edited by S. B. Ogale (Springer, Boston, MA, 2005).
- [7] A. Ohtomo and H. Y. Hwang, *Nature (London)* **427**, 423 (2004).
- [8] A. D. Caviglia, S. Gariglio, N. Reyren, D. Jaccard, T. Schneider, M. Gabay, S. Thiel, G. Hammerl, J. Mannhart, and J.-M. Triscone, *Nature (London)* **456**, 624 (2008).
- [9] A. D. Caviglia, M. Gabay, S. Gariglio, N. Reyren, C. Cancellieri, and J.-M. Triscone, *Phys. Rev. Lett.* **104**, 126803 (2010).
- [10] S. Gariglio, A. D. Caviglia, J.-M. Triscone, and M. Gabay, *Rep. Prog. Phys.* **82**, 012501 (2018).
- [11] Y.-Y. Pai, A. Tylan-Tyler, P. Irvin, and J. Levy, *Rep. Prog. Phys.* **81**, 036503 (2018).
- [12] J. Zhou, W.-Y. Shan, and D. Xiao, *Phys. Rev. B* **91**, 241302(R) (2015).
- [13] H. Thierschmann, E. Mulazimoglu, N. Manca, S. Goswami, T. M. Klapwijk, and A. D. Caviglia, *Nat. Commun.* **9**, 2276 (2018).
- [14] A. Annadi, G. Cheng, H. Lee, J.-W. Lee, S. Lu, A. Tylan-Tyler, M. Briggeman, M. Tomczyk, M. Huang, D. Pekker, C.-B. Eom, P. Irvin, and J. Levy, *Nano Lett.* **18**, 4473 (2018).
- [15] A. Jouan, G. Singh, D. C. Vaz, M. Bibes, A. Barthelemy, C. Ulysse, D. Stornaiuolo, M. Salluzzo, S. Hurand, J. Leseuer, C. Feuillet-Palma, and N. Bergeal, *Nat. Electron.* **3**, 201 (2020).
- [16] L. Fidkowski, R. M. Lutchyn, C. Nayak, and M. P. A. Fisher, *Phys. Rev. B* **84**, 195436 (2011).
- [17] C. A. Perroni, V. Cataudella, M. Salluzzo, M. Cuoco, and R. Citro, *Phys. Rev. B* **100**, 094526 (2019).
- [18] J. Settimo, F. Forte, C. A. Perroni, V. Cataudella, M. Cuoco, and R. Citro, *Phys. Rev. B* **102**, 224508 (2020).
- [19] M. Salluzzo, J. C. Cezar, N. B. Brookes, V. Bisogni, G. M. De Luca, C. Richter, S. Thiel, J. Mannhart, M. Huijben, A. Brinkman, G. Rijnders, and G. Ghiringhelli, *Phys. Rev. Lett.* **102**, 166804 (2009).
- [20] G. Berner, M. Sing, H. Fujiwara, A. Yasui, Y. Saitoh, A. Yamasaki, Y. Nishitani, A. Sekiyama, N. Pavlenko, T. Kopp, C. Richter, J. Mannhart, S. Suga, and R. Claessen, *Phys. Rev. Lett.* **110**, 247601 (2013).
- [21] M. Ben Shalom, M. Sachs, D. Rakhmilevitch, A. Palevski, and Y. Dagan, *Phys. Rev. Lett.* **104**, 126802 (2010).
- [22] B. J. van Wees, L. P. Kouwenhoven, E. M. M. Willems, C. J. P. M. Harmans, J. E. Mooij, H. van Houten, C. W. J.

- Beenakker, J. G. Williamson, and C. T. Foxon, *Phys. Rev. B* **43**, 12431 (1991).
- [23] Z. Zhong, A. Toth, and K. Held, *Phys. Rev. B* **87**, 161102(R) (2013).
- [24] G. Khalsa, B. Lee, and A. H. MacDonald, *Phys. Rev. B* **88**, 041302(R) (2013).
- [25] M. Vivek, M. O. Goerbig, and M. Gabay, *Phys. Rev. B* **95**, 165117 (2017).
- [26] Y. Fukaya, S. Tamura, K. Yada, Y. Tanaka, P. Gentile, and M. Cuoco, *Phys. Rev. B* **100**, 104524 (2019).
- [27] J. Ruhman, A. Joshua, S. Ilani, and E. Altman, *Phys. Rev. B* **90**, 125123 (2014).
- [28] F. Trier, D. V. Christensen, and N. Pryds, *J. Phys. D: Appl. Phys.* **51**, 293002 (2018).
- [29] C.-K. Wang and K. F. Berggren, *Phys. Rev. B* **54**, R14257(R) (1996).
- [30] S. Datta, *Electronic Transport in Mesoscopic Systems* (Cambridge University Press, Cambridge, 1995).
- [31] L. W. van Heeringen, G. A. de Wijs, A. McCollam, J. C. Maan, and A. Fasolino, *Phys. Rev. B* **88**, 205140 (2013).
- [32] L. W. van Heeringen, A. McCollam, G. A. de Wijs, and A. Fasolino, *Phys. Rev. B* **95**, 155134 (2017).
- [33] R. Winkler, *Spin-Orbit Coupling Effects in Two-Dimensional Electron and Hole Systems* (Springer, Berlin, 2003).
- [34] C. A. Perroni, D. Bercioux, V. Marigliano Ramaglia, V. Cataudella, *J. Phys.: Condens. Matter* **19**, 186227 (2007).
- [35] P. Iorio, C. A. Perroni, and V. Cataudella, *Eur. Phys. J. B* **89**, 97 (2016).
- [36] P. Iorio, C. A. Perroni, and V. Cataudella, *Phys. Rev. B* **95**, 235420 (2017).
- [37] V. Marigliano Ramaglia, D. Bercioux, V. Cataudella, G. De Filippis, C. A. Perroni, and F. Ventriglia, *Eur. Phys. J. B* **36**, 365 (2003).
- [38] V. Marigliano Ramaglia, D. Bercioux, V. Cataudella, G. De Filippis, and C. A. Perroni, *J. Phys.: Condens. Matter* **16**, 9143 (2004).
- [39] V. M. Ramaglia, V. Cataudella, G. De Filippis, and C. A. Perroni, *Phys. Rev. B* **73**, 155328 (2006).
- [40] B. I. Halperin, *Phys. Rev. B* **25**, 2185 (1982).
- [41] In this work, we assume the more realistic hard wall conditions on the x-dependent boundary, while in the experimental work [15], a 2D saddle potential is used for some estimations of QPC transport.
- [42] D. K. Ferry, S. M. Goodnick, and J. Bird, *Transport in Nanostructures*, 2nd ed. (Cambridge University Press, Cambridge, 2009).
- [43] L. P. Kouwenhoven, B. J. van Wees, C. J. P. M. Harmans, J. G. Williamson, H. van Houten, C. W. J. Beenakker, C. T. Foxon, and J. J. Harris, *Phys. Rev. B* **39**, 8040 (1989).
- [44] N. K. Patel, J. T. Nicholls, L. Martin-Moreno, M. Pepper, J. E. F. Frost, D. A. Ritchie, and G. A. C. Jones, *Phys. Rev. B* **44**, 10973 (1991).
- [45] L. I. Glazman and A. V. Khaetskii, *JETP Lett.* **48**, 591 (1988).
- [46] C. W. Groth, M. Wimmer, A. R. Akhmerov, and X. Waintal, *New J. Phys.* **16**, 063065 (2014).
- [47] T. E. Oliphant, *A guide to NUMPY* (Trelgol Publishing, 2006), Vol 1.
- [48] M. Wimmer, A. R. Akhmerov, J. P. Dahlhaus, and C. W. J. Beenakker, *New J. Phys.* **13**, 053016 (2011).
- [49] A. Maiellaro, F. Romeo, C. A. Perroni, V. Cataudella, and R. Citro, *Nanomaterials* **9**, 894 (2019).
- [50] F. Mireles and G. Kirczenow, *Phys. Rev. B* **64**, 024426 (2001).